



## Charge Transport Through Thin Amorphous Titanium and Tantalum Oxide Layers

Kevin Stella,<sup>a,\*</sup> Domocos A. Kovacs,<sup>a</sup> Detlef Diesing,<sup>a,z</sup>  
Wolfgang Brezna,<sup>b</sup> and Jürgen Smoliner<sup>b</sup>

<sup>a</sup>Fakultät für Chemie, Universität Duisburg-Essen, D-45117 Essen, Germany

<sup>b</sup>Institute of Solid State Electronics, Vienna University of Technology, Floragasse 7, A-1040 Vienna, Austria

Heterosystems of metal/insulator/gold type with titanium oxide and tantalum oxide as internal barriers are studied using internal photoemission (IPE), field induced current transport (current transients after voltage steps) and chemical reaction induced current transport (chemicurrent). IPE investigations over a broad energy range from 0.8 to 4.5 eV allow a determination of the interstitial layers band gap and the maximum height of the internal tunnel barrier. The built-in field of the heterosystem is derived by the evaluation of the slope in the photoyield versus photon energy plot. Current transients recorded after voltage steps allow the determination of the heterosystems time constants which generally have a value of some milli seconds. In titanium oxide systems additional time constants with values of several 100 s appear for bias voltages >0.5 V. These time constants are assigned to slow processes altering the height of the titanium oxide barriers.

© 2011 The Electrochemical Society. [DOI: 10.1149/1.3566194] All rights reserved.

Manuscript submitted July 26, 2010; revised manuscript received February 10, 2011. Published March 28, 2011.

Heterosystems with thin oxide layers are interesting for a variety of applications as thin film capacitors,<sup>1-3</sup> chemicurrent detectors<sup>4</sup> and electron sources in spin polarized tunneling.<sup>5</sup> In the present work we present a comparative investigation of charge transport induced by different methods through thin oxide films. Charges are driven through the oxide by: i) application of a device voltage ii) illumination of the samples with monochromatic light at variable photon energies, leading to spectra of internal photoemission, iii) non adiabatic chemical surface reactions. All three methods are combined since it is possible to derive the nature of excited carriers transport through heterosystems.<sup>6</sup> For aluminum and tantalum oxide heterosystems it was found, that they form a high pass filter for excited electrons and holes (defect electrons).<sup>4,6</sup> Since the height of the internal barriers for electrons and holes can be modified by an applied bias voltage, it became possible to characterize the spectra of excited charge carriers with energies below the vacuum barrier.<sup>7</sup> Bias voltages of up to 1 V could be applied to the system which had an internal barrier height of 3 eV.

To increase the detection efficiency for excited electrons traveling from the surface of a metal towards the bulk, one can either decrease the thickness of the top metal film of a heterosystem or one can reduce the height of the internal barrier. But with a decrease of the internal barrier the method of applying a bias voltage for tuning this barrier might become problematic, since tunnel currents become larger with lower barrier heights. Additionally, the influence of midgap states, impurities and remanent changes of the internal barrier might become more relevant for lower barriers.<sup>8,9</sup> These problems are addressed in the present work.

A comparison of metal/insulator/metal heterojunctions is presented with potentiostatically formed titanium and tantalum oxide as interjacent insulating layer. Titanium and tantalum oxide were chosen since both have bandgaps smaller than 4.5 eV.<sup>10</sup> For amorphous tantalum oxide values of 4.2 eV are typical<sup>11,12</sup> whereas crystalline samples show values of 3.9–4.5 eV.<sup>12,13</sup> Bulk titanium oxide values are for rutile 3.03 eV and for anatase 3.2 eV. For polycrystalline titanium oxide films 3.34–3.39 eV are typical values.<sup>14</sup> The electrochemical oxide formation is also well known in the literature.<sup>15-19</sup> The electrochemical preparation is described in Sec. II A based on potentiodynamic growth in acetate solution, followed by the preparation of the gold top electrodes in vacuum as described in II B. The gold top electrodes seem to form a more heterogeneous, open structure on titanium oxide than on tantalum oxide. The growth is monitored by in situ resistivity measurements during evaporation of the metal film.

### Sample Preparation

**Electrochemical oxidation.**—As heterojunctions we employed thin film Ta/TaO<sub>x</sub>/Au and Ti/TiO<sub>x</sub>/Au sandwich structures. The tantalum bottom electrode (2 mm × 20 mm) was prepared by a mini e-beam evaporator under ultra high vacuum conditions (UHV) as shown previously in Refs. 20 and 21 whereas the titanium bottom electrode (2 mm × 20 mm) was evaporated using a bent beam evaporator under UHV conditions.<sup>22</sup>

The insulating oxide layers were prepared by a localized electrochemical oxidation procedure in an electrolytic droplet cell.<sup>23-25</sup> In order to minimize parallel corrosion processes during the oxidation,<sup>26</sup> a sodium acetate buffer electrolyte and an ammonium acetate buffer electrolyte (0.9 mol/l) were used for Ta and Ti, respectively. While an initial potential  $E_i = -1.0$  V is applied no chemical reaction takes place on Ta. For the Ti samples a slight increase of the negative current can already be seen for electrode potentials  $E_{SCE} < -0.8$  V. This can be attributed to a beginning hydrogen evolution at the Ti sample. The anodic oxidation is then initiated by increasing the potential with a constant rate  $dE_{SCE}/dt = 0.1$  V/s up to a final value  $E_f$ . In the present work, tantalum films oxidized at  $E_f = 2$  V as well as titanium films oxidized at  $E_f = 2$  V and  $E_f = 3$  V were used. The corresponding cyclovoltammograms, recorded during the oxidation of the Ta and Ti films, covered by a thin native oxide due to previous exposure to ambient air, are shown in Fig. 1. In all three cases, a similar behavior can be observed: up to a certain positive potential  $E_{I=0}$  the current density remains low, then it increases and goes through a maximum, and finally reaches a constant plateau value of some 10  $\mu$ A until  $E_f$  is reached. At a constant value of  $E_f$ , the current drops exponentially to zero within a few seconds. The so-called half wave potential  $E_{1/2}$  is usually introduced as a characteristic quantity describing the oxidation process, being defined as the potential at which the current density is half of its plateau value. For tantalum,  $E_{1/2}$  is of about +0.5 V, while for titanium it is around +1.0 V. The small difference in  $E_{1/2}$  between the two titanium samples is caused by a thicker gas phase oxide due to a longer exposition to ambient conditions after evaporation for the sample in the middle graph of Fig. 1.

One advantage of this oxidation procedure is the fact that it allows to control the oxide thickness  $z_{ox}$  by varying  $E_f$ , since the relation between the two quantities is approximately linear.<sup>27</sup> From this linear dependence, the so-called formation factor  $dz_{ox}/dE_f$  was found to be in the range 1.3–2.4 nm/V for TaO<sub>x</sub> (Ref. 19) and 1.3–3.3 nm/V for TiO<sub>x</sub>.<sup>19</sup> For our devices, we derived, from XPS sputter profiles, formation factors of about 2.2–2.4 nm/V for the tantalum and the titanium oxide, respectively. This calibration factor gives the thicknesses for the oxide layers of 4.4 nm (TaO<sub>x</sub>) and of 4.8–7.2 nm (TiO<sub>x</sub>).

\* Electrochemical Society Active Member.

<sup>z</sup> E-mail: detlef.diesing@uni-due.de

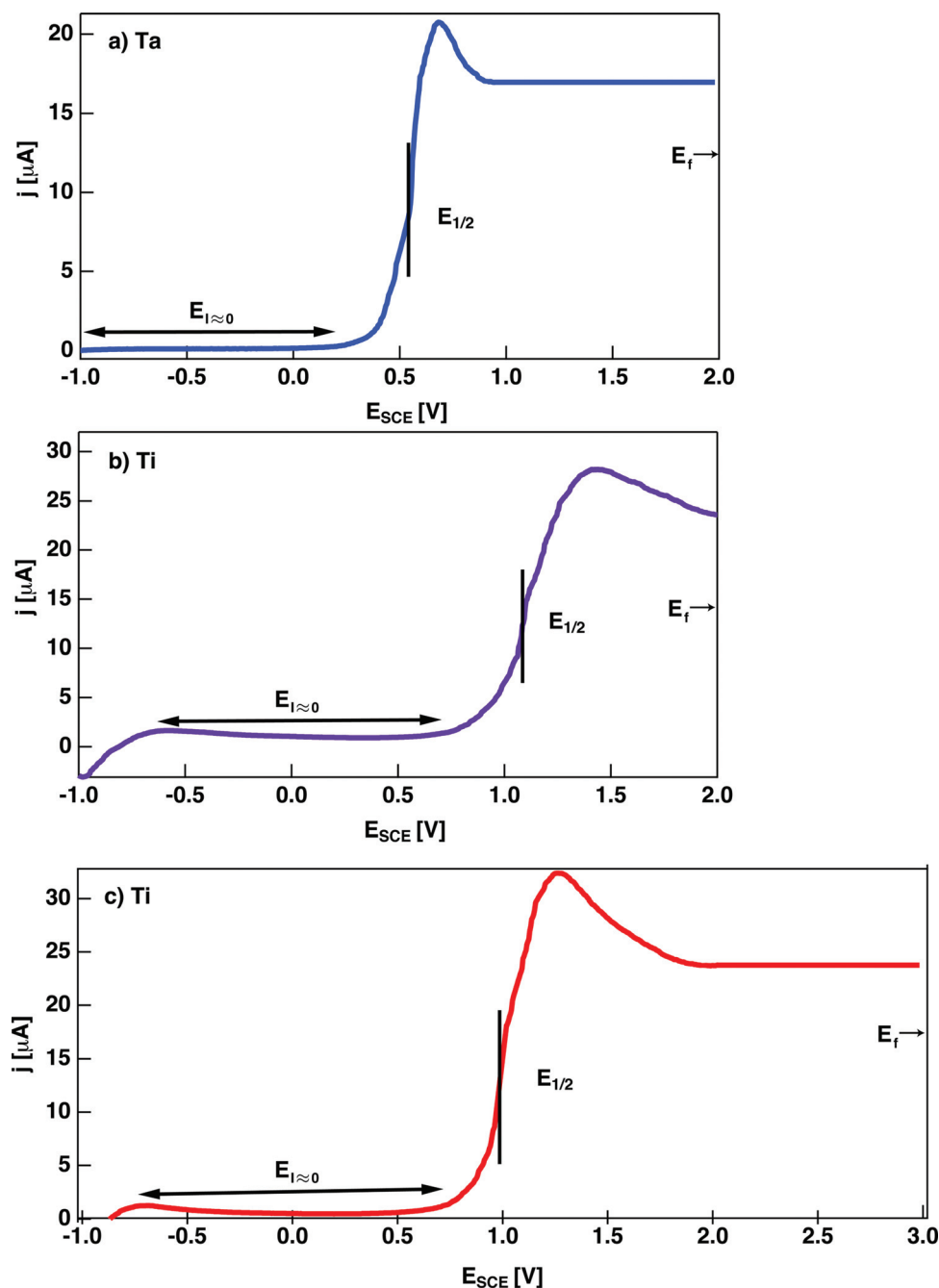


**Figure 1.** (Color online) Typical cyclic voltammograms ( $E_i = -1.0$  V and  $E_f = 2.0$ – $3.0$  V) recorded during the localized electrochemical oxidation in an electrochemical droplet cell of a tantalum (upper graph), and a titanium (middle and lower graph) substrate over an area  $A_{ox} \approx 4$  mm<sup>2</sup>, respectively, where  $E_{1/2}$  denotes the half wave potential.

**Evaporation of gold top electrodes.**—The gold top electrode (6 mm  $\times$  9 mm) was obtained by thermal evaporation at a rate of 0.3 nm/min under UHV conditions (base pressure  $< 10^{-8}$  mbar) across the oxide layer. The bottom and the top electrode were contacted with micrometer thick silver strips similar to Ref. 28.

The twofold contacts of the top electrode allow an in situ monitoring of the gold film's resistivity during its growth. In Fig. 2 the specific resistivity of the gold films (measured at 300 K) is plotted for thicknesses below 20 nm. The amount of gold evaporated on the sample was determined by a quartz balance. The x-axis in Fig. 2 is calibrated in the following way: Three different amounts of gold were evaporated on a glass substrate. The gold films on the glass were scratched, and their thickness was determined by measuring the average scratch depth from AFM line scans performed across the scratches. Hence, the x-axis in Fig. 2 is normalized to the growth of gold on glass.

Obviously films grown on titanium oxide have a comparable high specific resistivity. Gold films on tantalum oxide reach the

same resistivity values at thickness values which are 5.3 nm lower. At 20 nm thickness the specific resistivity of gold on tantalum oxide is  $1.4 \times 10^{-5}$   $\Omega$  cm, this value is indicated on the y-axis of Fig. 2 as well as the bulk value for gold  $\rho_{\text{bulk}}(\text{Au}) = 2.2 \times 10^{-6}$   $\Omega$  cm (Ref. 29). The gold films on glass, which were used for the calibration of the x-axis in Fig. 2 show a much lower resistivity. Increasing the thickness from 6.5 to 8 nm leads to a considerable resistivity decrease of five orders of magnitude.

The apparent differences in the gold film growth on the three substrates can be partially discussed with classical arguments for the thermodynamics of interfaces. One crucial parameter determining the film growth is the surface free energy  $\gamma$  of the adlayer and the substrate.

Titanium oxide has a low value of surface free energy  $\gamma$  of 0.35 J/m<sup>2</sup> (Ref. 30) whereas most metals show higher values. The range of values for metals is from  $\gamma = 0.4$  J/m<sup>2</sup> for lead<sup>31</sup> to  $\gamma = 1.4$  J/m<sup>2</sup> for gold<sup>32,33</sup> and  $\gamma \approx 2$ – $3$  J/m<sup>2</sup> for platinum.<sup>34,35</sup> To the authors

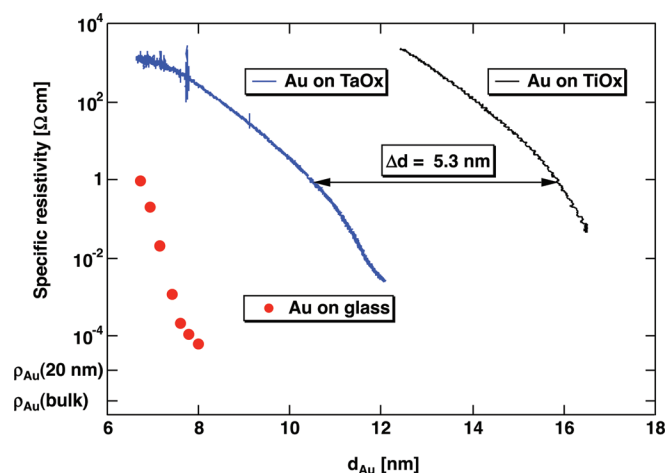


**Figure 2.** (Color online) Resistivity of the Au film evaporated on tantalum oxide, titanium oxide and on glass (measured at 300 K).  $\rho_{\text{bulk}}(\text{Au}) = 2.2 \times 10^{-6} \Omega \text{ cm}$  for  $T = 300 \text{ K}$  from<sup>29</sup> and the final resistivity for a 20 nm thick gold film on tantalum oxide are indicated on the y-axis.

knowledge, for tantalum oxide there is only one value in literature of  $\gamma = 0.28 \text{ J/m}^2$  which is cited in Ref. 30. When the surface free energy of the oxide  $\gamma_{\text{oxide}}$ , the surface free energy of the metal  $\gamma_{\text{metal}}$  and the interfacial energy  $\gamma_{\text{interface}}$  fulfill the inequality

$$\gamma_{\text{interface}} > (\gamma_{\text{oxide}} - \gamma_{\text{metal}}) \quad [1]$$

one expects cluster growth.<sup>36,37</sup> With the above mentioned values the right hand side of Eq. 1 will be negative for gold on titanium and tantalum oxide.  $\gamma_{\text{interface}}$  itself might only have a negative value if a chemical reaction happens between the gold and the oxide. This is unlikely for gold-titanium oxide interfaces.<sup>38</sup> For gold-tantalum-oxide interfaces the reaction of gold with the oxide is even more unlikely since the binding energy of tantalum oxide is higher. The binding energy for tantalum oxide is 201 kJ/mol,<sup>39</sup> for titanium oxide the value is 47.7 kJ/mol.<sup>40</sup> Hence, for both oxide-metal systems  $\gamma_{\text{interface}}$  can be expected to be positive leading to a tendency for cluster growth of gold on both oxides. This tendency should be weakest for gold on glass, since  $\gamma$  for glass surfaces is  $\approx 1 \text{ J/m}^2$ . This value is 2–3 times higher than the values for titanium oxide and tantalum oxide and leads to a lower negative value for the right hand side of Eq. 1. So, the comparative low resistivity values for gold on glass can be motivated by the high  $\gamma$  value for glass surfaces.

All these considerations are valid only when one considers the surface free energies. But several complicated effects might influence this simple consideration.

- Adsorbates or defects on the oxide surface may influence the value of  $\gamma$ .<sup>41</sup> In our case a partial hydroxide coverage of the electrochemically built oxide cannot be excluded.<sup>42,43</sup>
- A pure description in terms of interfacial energies might be insufficient since charge transfer processes between the adlayer and the substrate may induce a big interfacial stress.<sup>44,45</sup> This stress (not included in Eq. 1) can influence the growth mode of the adlayer significantly.<sup>46</sup>

In conclusion, we can not debate on the differences between gold on tantalum oxide and titanium oxide with thermodynamical values of surface and interface energies from literature. A tentatively closed structure of gold on glass can be rationalized by the high  $\gamma$  value of glass. A more open structure of the gold film on titanium oxide with a higher fraction of voids is suggested. This argument will be supported by chemcurrent experiments in Sec. V.

## Internal Photoemission

**Optical properties of the layer system.**— The optical properties of the layer system were calculated following the approaches of Edwards and Pepper.<sup>47,48</sup> The Fresnel equations are evaluated for normal incidence, taking into account the bulk dielectric properties of the oxide layers<sup>49–52</sup> and of the metals.<sup>53</sup> Deviations from the bulk dielectric properties of the oxide and metal layers are not taken into account in the present work. For that purpose one would need an in-situ ellipsometric control of the films during growth.<sup>54,55</sup>

In Fig. 3 the absorptivities in each layer as well as the total transmissivity and reflectivity of the total system are shown. For low photon energies  $h\nu < 2.5 \text{ eV}$  the absorptivity in the titanium respectively tantalum backelectrode is larger than in the gold top electrode. For both layer systems the absorptivity in the gold top electrode dominates for  $h\nu > 2.7 \text{ eV}$ . The dotted vertical lines in Fig. 3 indicate the photon energy where absorptivities in both metal electrodes are equal. Tantalum oxide does not show any significant absorptivity over the whole energy range, whereas titanium oxide shows values of up to 10% for  $3.5 \text{ eV} < h\nu < 4.5 \text{ eV}$ . This is considered to be due to the lower band gap of titanium oxide of 3.6 eV.<sup>56</sup> Interband excitation processes will dominate in this energy range.<sup>57</sup>

From a simple viewpoint, considering isotropic propagation of photoexcited carriers in the metal electrodes and over the oxide barrier, one should expect a polarity change of the photoinduced current at medium photon energies, e.g.  $\approx 2.5$ – $2.6 \text{ eV}$ . Anisotropies in the propagation of the photoelectrons as for example induced by

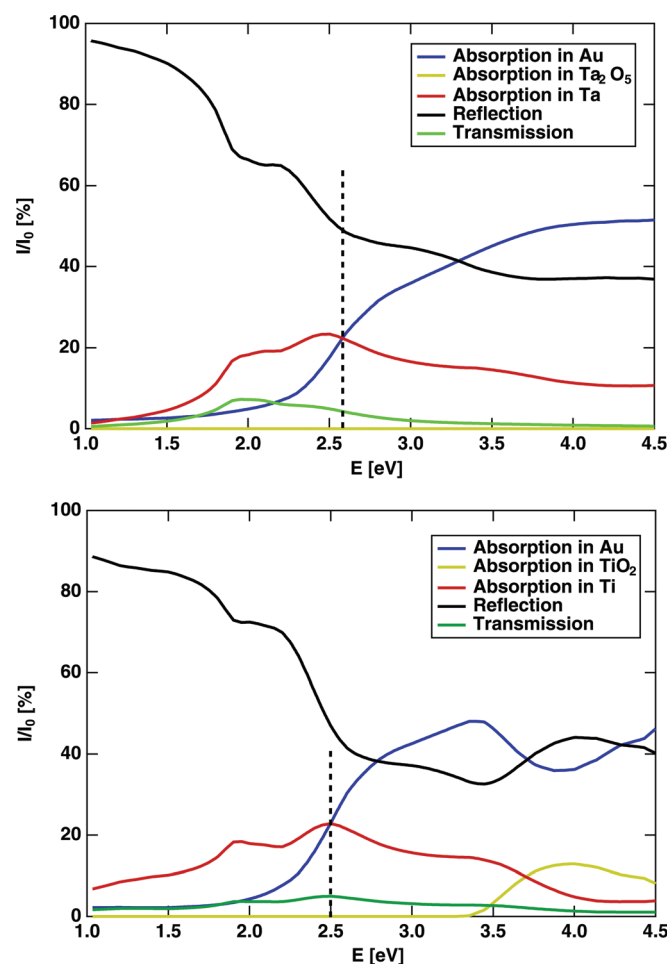


**Figure 3.** (Color online) Absorptivities for the tantalum oxide (upper graph) and the titanium oxide (lower graph) based devices. The dotted lines indicate the photon energies with equal absorptivities in the top and in the back electrode.

built-in internal electric fields may significantly alter the frequency dependence of the photon yield.<sup>58</sup>

A layer system with a built-in field directed towards the top electrode is shown in Fig. 4. Scattering processes with optical phonons may occur when excited carriers pass the oxide layer. This leads to energy losses of several 100 meV.<sup>59,60</sup> These energy losses hamper the transport of electrons travelling against the built-in field. After the scattering these electrons have a much lower tunnel probability, see path with red arrow from the left to the right hand side in Fig. 4. On the other hand, photoelectrons from the top electrode directly have to tunnel. Scattering processes during the subsequent transport in the oxide's conduction band then only have a minor effect because the transport to the conduction band of the bottom electrode is not hindered by a further barrier, see path with blue arrow from the right to the left hand side in Fig. 4.

It should be mentioned that electron-phonon (e-ph) scattering causes a higher energy loss in the oxide than in the metal since in the oxide the contribution of optical phonons dominates whereas acoustical phonons are the main scatterers in the metals. However, the above mentioned 'directional effect' of the oxides internal field will only work when the mean free path for the e-ph scattering in the oxide is in the range or below the oxide thickness. This seems to be valid since values of 0.4–0.6 nm for the mean free path were found.<sup>61–63</sup>

**Optical setup.**— As a light source for our high-energy photon studies we employed a Xe lamp in connection with a monochromator which produces a monochromatic beam of radiation with selectable photon energies in the range between 1.1 and 4.1 eV, i.e. wavelengths of 300–1100 nm. The linewidth of the beam was about 5 nm. The beam was guided to the MIM device by means of a 2 mm thick quartz fiber, whose end was mounted close to the sample to avoid the illuminated area becoming larger than the active area as a result of beam divergence. The flux of photons impinging on the gold surface was calibrated by employing a silicon photodiode of known sensitivity.

For the low-energy photon studies (e.g. photon energies between 0.8 and 1.3 eV) the variable wavelength light source consisted of a quasi continuous wave (CW) high power white laser source, a Koheras Versa connected to a Czerny-Turner Monochromator (Triax180 by Horiba Jobin Yvon). Similar to the high-energy photon

studies, a multimode fibre was used to deliver the monochromatic light to the MIM device. Again, care was taken to illuminate only the active area of the MIM device. Due to the low excitation energies, a sub-fA Source Measure Unit (Keithley Model K6430) had to be used to measure the subsequent low excited currents in the pA range at 0 V applied bias. To avoid influence from external stray fields and external light, all measurements were carried out inside a shielding box.

Current measurements were performed by means of a HEKA potentiostat which incorporates a current-to-voltage converter with a conversion factor of 10 mV/pA. The Potentiostat did also supply the dc bias voltage applied between the top gold electrode and the bottom metal layer. The measured current is defined as the net number of detected electrons in the bottom electrode (Ta or Ti) per unit time. A negative current then means a net current of electrons flowing from the bottom into the top metal electrode. The photon-induced electron emission is characterized by a yield

$$\gamma = \frac{\text{detected photo current}}{\text{impinging photon flux}}$$

defined as the average number of detected electrons induced by one incoming photon. The wavevector of the incident light was parallel to the surface normal of the samples.

**Experimental results.**— The photoyield  $\gamma$  as a function of photon energy is shown in Fig. 5. It should be mentioned that for an applied bias of 0 V the yield always shows positive values in the whole energy range. This means that a net photoelectron current flows from the top electrode to the back electrode. A polarity change cannot be observed, despite the fact that for energies  $h\nu < 2.5$  eV more carriers are photoexcited in the bottom electrodes titanium or tantalum (see Fig. 3). Hence, the directional effect of the built-in electric field seems to work in both types of devices at 0 V bias voltage.

In the upper graph of Fig. 5 the photoyield is plotted linearly. Strong increases of the photoyield are observed for  $h\nu > 3.6$  eV for titanium oxide and  $h\nu > 4$  eV for tantalum oxide. The inset in the upper graph shows the square root of the photoyield according to Fowler's analysis of photoemission.<sup>64</sup> This approach calculates  $\gamma$  as

$$\gamma \propto (h\nu - \Phi)^2 \quad [2]$$

where  $\Phi$  is the workfunction in conventional photoemission or the height of the internal barrier in internal photoemission.

So, for high energies the square root of the photoyield  $\gamma$  is approximated by line fits, the intersection of the line fits with the energy axis is used as an estimation for the band gap as suggested in Refs. 65 and 56. Values of 3.4 and 3.9 eV are evaluated for titanium and for tantalum oxide.

The analysis of our data according to the laws of interfacial electron transfer in metal-liquid systems (sometimes cited as 5/2 law of photoelectrochemistry<sup>66–69</sup>) does not seem to be appropriate since the charge transfer occurs between two solid phases of our system.

In the lower graph the photoyield is scaled logarithmically. For both devices regions with different slopes can be distinguished. For photon energies  $h\nu < 0.8$  eV no signal could be detected. In this case the carriers have to tunnel through the entire length of the oxide layer (see process (IR) in Fig. 4). From 0.8 to 1.3 eV a steep slope can be observed for titanium oxide samples, for tantalum oxide systems up to 2.0 eV. For these photon energies tunnel processes through the upper edge of a triangular tunnel barrier can be discussed similarly to the Fowler-Nordheim mechanism.<sup>70,71</sup> For this purpose a tilted barrier with

$$E_{bar}(z) = E_0 + \left(\frac{z}{d_{oxide}}\right)E_b \quad [3]$$

with different values of  $E_0$  is assumed.  $E_0$  is the barrier height at the titanium-titanium oxide or at the tantalum-tantalum oxide interface

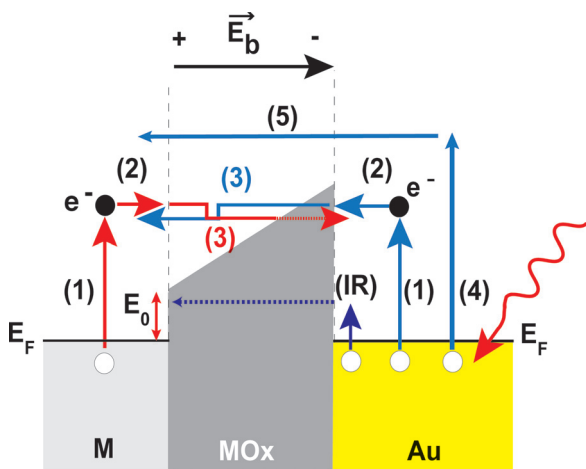


**Figure 4.** (Color online) Schematic drawing of a metal-insulator-metal device and the built-in field  $\vec{E}_b$ . (IR) denotes photo excitation with  $h\nu < 1$  eV, the electron has to tunnel through the whole oxide. Process (1) denotes photo excitation for  $1 \text{ eV} < h\nu < 2 \text{ eV}$ . Process (2) assigns the transport to the interface. Process (3) denotes transport through the oxide with energy loss due to electron-phonon interaction leading to a lower tunnel probability for electrons going from the left to the right. Processes (4) and (5) denote over the barrier excitation and transport.  $E_0$  denotes the lower height of the potential barrier at the backelectrode (titanium or tantalum)/oxide interface.



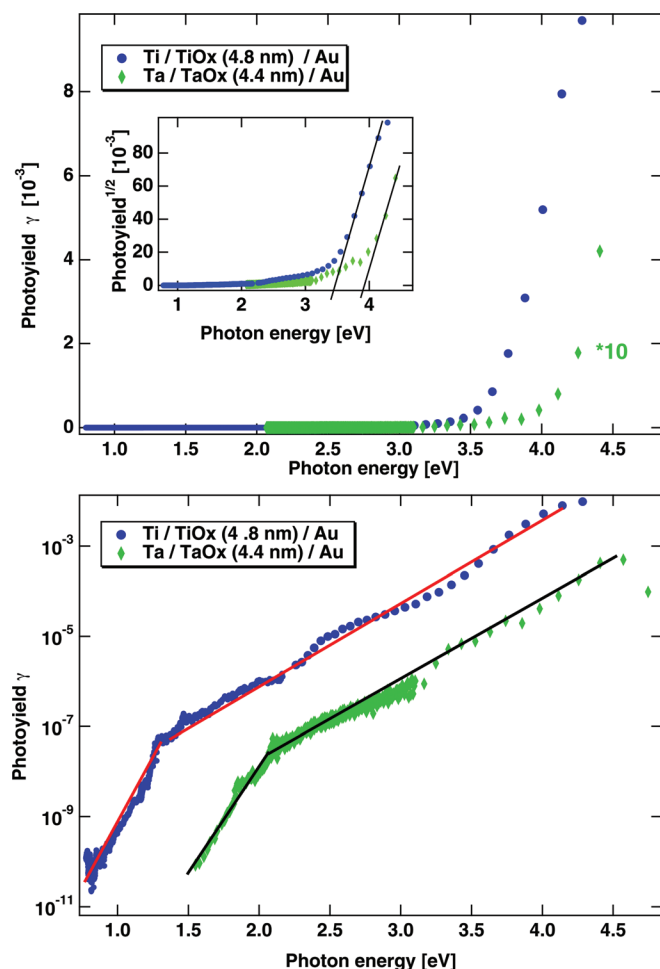


**Figure 5.** (Color online) Upper graph: Photocurrent for Ti/TiO<sub>x</sub>(4.8 nm)/Au and Ta/TaO<sub>x</sub>(4.4 nm)/Au junctions plotted linearly. Inset shows the square root of the photocurrent as function of photoenergy. The intersection of the line fits with the x-axis indicate the band gaps of the respective oxides. Lower graph: Logarithmic plot of the internal photoemission yield as a function of the incident light energy for zero volt bias.  $sl_1$  and  $sl_2$  denote the different slopes in the logarithmic plot.

respectively, see Fig. 4.  $z$  denotes the coordinate normal to the system interfaces with  $z=0$  at the titanium–titanium oxide or at the tantalum–tantalum oxide interface.  $d_{\text{oxide}}$  denotes the thickness of the oxide. The barrier height at the opposed oxide interface (oxide–gold) is  $E_0 + E_b$ .  $E_b$  causes the unbalance of the oxides conduction band in Fig. 4. The unbalance of the conduction band evokes a built-in electric field  $\vec{E}_b$  whose absolute value is given by

$$|\vec{E}_b| = \frac{E_b}{d_{\text{oxide}}} \quad [4]$$

The evaluation of the slope  $sl_1$  can now be used to determine the unknown value for  $E_b$  by a simple iteration.

The tunnel probability  $T(E)$  through the tilted barrier  $E_{\text{bar}}(z)$  can be expressed by the Wentzel-Kramers-Brillouin (WKB) approach<sup>72–74</sup> as

$$T(h\nu) = \exp \left\{ -\kappa \left[ \left( \int_0^{d_{\text{oxide}}} \sqrt{h\nu - E_{\text{bar}}(z)} dz \right) \right] \right\} \quad [5]$$

with

$$\kappa = \sqrt{\frac{2m}{\hbar^2}}$$

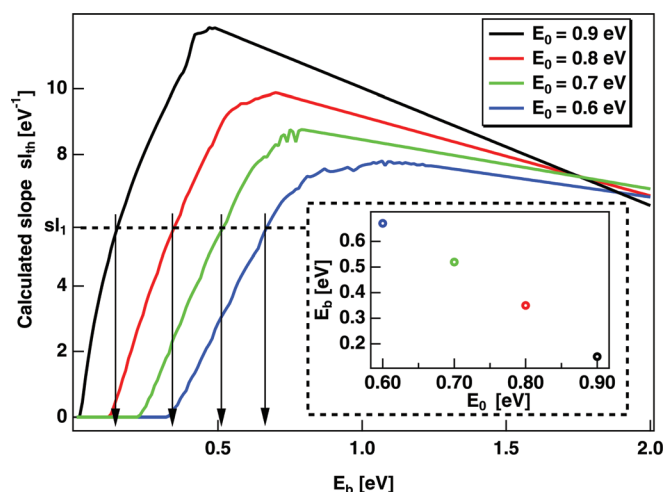


**Figure 6.** (Color online) Calculated slope values according to Eq. 6. Experimental value  $sl_1 = 5.8$  is denoted in the y-axis. Vertical arrows point to values of  $E_b$  which fit to  $sl_1$ . Inset shows the combination of  $E_0$  and  $E_b$  values which fit to experimentally determined  $sl_1$ .

With Eq. 5 one can evaluate the partial derivative

$$\left. \frac{\partial \log(T(h\nu))}{\partial h\nu} \right|_{h\nu_1}^{h\nu_2} = sl_{th} \quad [6]$$

The theoretically found values  $sl_{th}$  have to be compared with the experimentally found slope values  $sl_1$ . Equation 6 is evaluated for  $h\nu_1 = 0.9$  eV and  $h\nu_2 = 1.3$  eV for titanium, while for tantalum  $h\nu_1 = 1.6$  eV and  $h\nu_2 = 1.9$  eV are used.

The calculated values of  $sl_{th}$  are shown in Fig. 6 for different values of  $E_0$ . The intersection of the calculated curves with the horizontal line given by  $sl_{th} = sl_1$  gives possible values for the internal field  $E_b$ . The relation between  $E_0$  and  $E_b$  is shown in the inset of Fig. 6. The relation shows that the evaluation of the experimental results in Fig. 5 reached by the ratio of tunnel probabilities allows a determination of value pairs for  $E_0$  and  $E_b$ . In table 1 the results from the evaluation of  $sl_1$ ,  $E_0$  and  $E_b$  are listed.

From the data presented here it is on the first glance difficult to discriminate between the value pairs  $E_0$  and  $E_b$  fulfilling Eq. 6. However, for the tantalum–tantalum oxide–gold system one can find an argument for values of 1.0 and 0.63 eV for  $E_0$  and  $E_b$ . The value of 0.63 eV lies near to the difference of work functions for tantalum and gold of 0.7 eV, a value which was already found by R. H. Fowler.<sup>64</sup> We state that these values coincide by chance, since the structure of the barrier is influenced for example by dipole layers at the interfaces and the hydroxide layer at the tantalum oxide–gold interface.<sup>42</sup> However, newer works about the dependence of the internal photoemission on the top electrode's thickness point also to a value of 0.6 until 0.7 eV for  $E_b$ .<sup>75</sup> So we think that a value of around 0.6 eV for  $E_b$  might be valid for both oxide systems in all likelihood.

**Table I.** Evaluation of the exponential dependence of the photocurrent  $\gamma$  as function of  $h\nu$  (see Figs. 5 and 6)  $E_0$  and  $E_b$  are value pairs fulfilling Eq. 6.

$sl_1$		Titanium 5.8		Tantalum 5.2	
$E_0$	$E_b$	0.6	0.67	1.0	0.63
$E_0$	$E_b$	0.7	0.52	1.1	0.50
$E_0$	$E_b$	0.8	0.35	1.2	0.41
$E_0$	$E_b$	0.9	0.15	1.3	0.29

For higher photon energies, i.e.  $h\nu > 2$  eV,  $\gamma$  shows again a linear behaviour in the logarithmic plot, but for both tantalum and titanium systems with a flatter slope. Interestingly the slopes in these two regions are very similar for both types of devices. The flat slope ( $sl_2 \approx 1.9 < 0.5 sl_1$ ) represents a weaker energy dependence. The evaluation procedure applied above following Eqs. 6 and 5 leads to barrier heights of 9 eV. Obviously, this is not a meaningful value for a barrier height within our systems. The highest threshold energy is the band gap of the oxides of 3.4 and 3.9 eV as determined in the inset of the upper graph in Fig. 5.

An interpretation of  $sl_2$  is in the present time not easy, additionally the value of  $sl_2$  is valid over a wide range of photon energies from 2 to 4 eV. Photoelectrons with these energies are transported in the conduction band. Thus, the low value of  $sl_2$ , expressing a low energy dependence, might point to a scattering dominated transport in the conduction band. For tantalum oxide this transport does not depend on bias voltages up to 0.2 eV. Also both slope values  $sl_1$  and  $sl_2$  remain constant.

This is different for titanium oxide samples. Here the photoyield  $\gamma$  depends clearly on the applied bias, especially for the medium photon energy range from 2 to 4 eV as shown in Fig. 7. This Fig. shows the logarithmic plot of the photoyields  $\gamma$  of a Ti/TiO<sub>x</sub>(4.8 nm)/Au sample and a Ti/TiO<sub>x</sub>(7.2 nm)/Au sample. The photoyields show slightly lower values for the sample with the thicker oxide layer at 0 V bias. The thickness dependence is much more pronounced for applied biases. With a bias of +0.1 V  $\gamma$  values of  $10^{-4}$  for the 4.8 nm sample decrease to  $4 \times 10^{-5}$  for the 7.2 nm samples. For a negative bias voltage even a polarity change of the photoinduced current can be observed. With photon energies  $h\nu > 3.5$  eV the net photoelectron current flows from the gold top electrode to the titanium back electrode, the net current flows in the opposite direction for  $h\nu < 3.5$  eV. The insets of Fig. 7 show linear plots of  $\gamma$  where negative values appear with nearly no dependence on the photon energy. With the negative bias voltage,  $\gamma$  shows also a pronounced thickness dependence for these photon energies.  $\gamma$  decreases from  $-5 \times 10^{-4}$  for the 4.8 nm sample to  $-2 \times 10^{-4}$  for the 7.2 nm sample.

Hence, for both bias voltages  $\pm 0.1$  V the exponential increase of the photoyield  $\gamma$  from  $h\nu = 2$  eV to  $h\nu = 3$  eV vanishes and is replaced by a more or less constant photoyield. The ratio of the photoyield  $\gamma(U_T = 0.1$  V) and  $\gamma(U_T = 0.0$  V) is shown in Fig. 8. The ratio seems to increase exponentially with decreasing photon energies down to 2 eV and reaches values of up to 80. An analysis with photon energies below 2 eV was not possible. The photosignal induced by the chopped beam from the monochromator was overlaid by a significant fluctuation of the dark current signal. Experiments with a temperature stabilized setup are under way to avoid these difficulties.

It should be mentioned that experiments in this range of photon energies (2–4 eV) cannot be explained with the previously discussed values for the barrier height  $E_0$  or the internal field  $E_b$ . Carriers with these excess energies  $h\nu > E_0 + E_b$  will be transported predominantly in the conduction band. Thus, it seems to be surprising that such a low bias voltage drastically influences the transport in the band. But one can think about a temperature activated hopping conduction. Activated conduction processes which can be influenced by small electric fields may happen in the band, similar to conduction on the edge of the conduction band as known in the so called Urbach tails.<sup>76–78</sup> The influence of the field is large for photon energies of 2 eV, meaning conduction processes at the edge of the band. With higher photon energies the influence of the field becomes weaker and vanishes nearly for 4 eV (see Fig. 8).

### Bias-Induced Charge Transport

**Current driven by voltage ramps.**— Figure 9 depicts the typical current–voltage (*I*–*U*) characteristics of the Ta/TaO<sub>x</sub>/Au and Ti/TiO<sub>x</sub>/Au samples, recorded at a constant rate  $dU/dt = 20$  mV/s in the voltage range between  $-0.2$  and  $+0.2$  V. For an ideal metal/in-

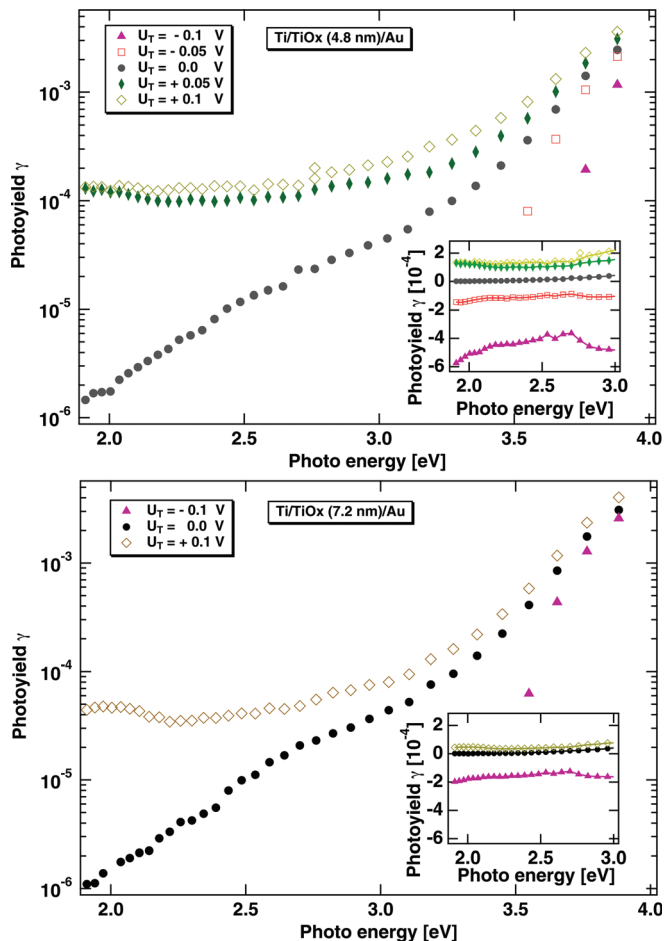


**Figure 7.** (Color online) Logarithmic plot of the internal photoemission yield as a function of the incident light energy for several bias voltages applied to the titanium back electrode. Upper graph: Ti/TiO<sub>x</sub>(4.8 nm)/Au sample. Lower graph: Ti/TiO<sub>x</sub>(7.2 nm)/Au sample. The inset shows a zoom of the photoemission yield plotted linear for photon energies of 1.9–3 eV.

ulator/metal system, the tunneling current  $I_T$  should be very small for bias voltages  $U_T$  with  $eU_T < E_0$ , with  $E_0$  being the lowest potential barrier in the heterosystem (see Fig. 4). In this case, the current response to the constant voltage ramp is only given by the time dependent (de-) charging current according to

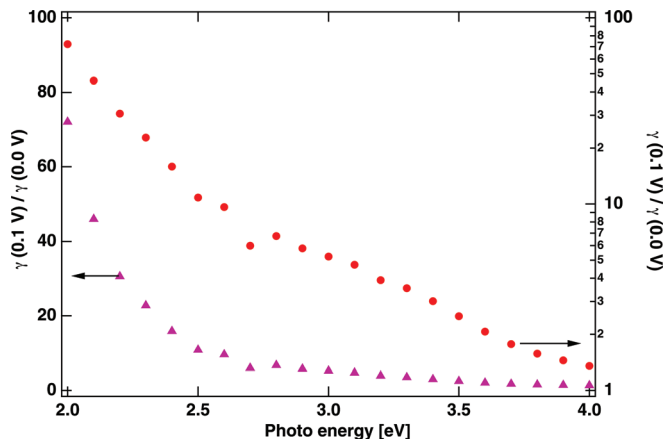


**Figure 8.** (Color online) Influence of the bias on the photoyield: Ratio of photoyields  $\gamma(0.1$  V) and  $\gamma(0.0$  V) for the Ti/TiO<sub>x</sub>(4.8 nm)/Au sample.

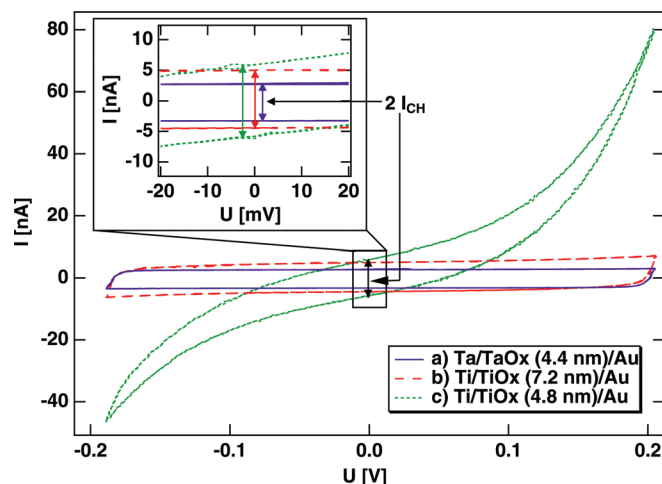


**Figure 9.** (Color online) Current-voltage curves of a) Ta/TaO<sub>x</sub> (4.4 nm)/Au, b) Ti/TiO<sub>x</sub> (7.2 nm)/Au and c) Ti/TiO<sub>x</sub> (4.8 nm)/Au recorded at a constant rate  $dU/dt = 20$  mV/s.  $I_{CH}$  is the charging current according to Eq. 7.

$$C = \frac{Q}{U} = \frac{\frac{dQ}{dt}}{\frac{dU}{dt}} = \frac{I_{CH}}{\frac{dU}{dt}} \quad [7]$$

Here,  $C$  is the capacitance introduced by the oxide layer,  $I_{CH}$  is determined as shown in Fig. 9. According to Eq. 7, the Ta/TaO<sub>x</sub>(4.4 nm)/Au, Ti/TiO<sub>x</sub>(4.8 nm)/Au and Ti/TiO<sub>x</sub>(7.2 nm)/Au samples have capacitances of 148, 300, and 235 nF, respectively. Taking into account the resistivity of the gold top electrode  $R_{Au} \approx 50 \Omega$  and the titanium back electrode  $R_{Ti} \approx 400 \Omega$ , one can derive a time constant  $\tau$  of the system as  $\tau = RC \approx 1$  ms.

Ta/TaO<sub>x</sub>(4.4 nm)/Au and Ti/TiO<sub>x</sub>(7.2 nm)/Au exhibit, according to Fig. 9, a nearly ideal behavior. A strong deviation from this behavior can be observed in the case of Ti/TiO<sub>x</sub>(4.8 nm)/Au. In this case an exponential dependence of the current on the bias voltage can already be seen. Since this exponential shape does not appear for the thicker titanium oxides, one could explain this by an increased tunnel probability through the thinner oxide. A detailed discussion will be given in the Sec. IV C.

**Transient shape of the device current.**— The transient shape of the device current after voltage steps allows the determination of the system's time constants in a more detailed way than the quasistationary current voltage method mentioned above. In the present work we use a system with dynamically switching current-voltage converter at 0.1 and 1 s after the application of a voltage step. Thus, in one experiment one can measure the above determined time constants with currents of several mA as well as tunnel currents of some 100 pA for a long time. It is the aim of this section, to clearly separate the macroscopic time constants of the heterosystem as mentioned above (with a charge flow of some microcoulomb) from long term drifts (with a charge flow of some pC). The latter ones may drastically influence the performance of chemcurrent and photocurrent measurements since the observed currents are in the pA range.<sup>4,79</sup>

The experiment is conducted in the following way. The gold top electrode is always held on ground potential. The potentials indicated in the following figures are applied to the titanium backelectrode. The initial potential  $E_{ini}$  is 0 V. The final potential  $U_{step}$  is positive on the titanium back electrode. We have chosen this polarization with an electron flow from the gold top electrode to the titanium back electrode since the net photoelectron current studied in Sec. III C flows in the same direction.

In Fig. 10 the transient shape of the device current after voltage steps from 0 V to the voltages  $U_{step}$  indicated in the figure are

shown. The dotted line is a calculated charging curve of a capacitance ( $C_{ox} = 250 \mu\text{F}$ ) and a serial resistance ( $520 \Omega$ ) according to

$$i(t) = \frac{U_{step}}{R_{serial}} \left( e^{-\frac{t}{R_{serial}C_{ox}}} \right) \quad [8]$$

The values of  $C_{ox}$  and  $R_{serial}$  correspond to the capacity of the oxide layer and the sum of the resistivities of the titanium base and the gold top electrode. Obviously, the transient shape of the current is dominated by the capacitive charging in the first  $10^{-3}$  s since the experimental curves and the calculated charging curve coincide quite well. From  $t = 10^{-3}$  s to  $t = 10^1$ – $10^2$  s a linear decay in the double logarithmic plot with a slope

$$\frac{\partial \log(I)}{\partial \log(t)} = -0.95 \pm 0.03 = \alpha$$

points to a power law like decay according to  $I \propto t^\alpha$ . Such a kind of behavior is often found in thin vitreous oxide films<sup>80–82</sup> and was for the first time studied by J. Curie<sup>83</sup> and E. R. von Schweidler.<sup>84</sup> With  $U_{step} = 0.3$  V a detectable current remains even after  $10^3$  s.

With higher step voltages the remanent current increases and reaches a constant level after 10 or 100 s for voltages of 0.5 and 0.4 V respectively (see Fig. 11). A different behaviour appears for  $U_{step} > 0.5$  V. The current is at a minimum value at around  $t = 10$  s but then increases again, and reaches a constant value after more than  $5 \times 10^4$  s. The current transient for  $U_{step} = 0.7$  V is plotted in the inset of Fig. 11 in linear scale. Its shape is proportional to  $1 - \exp(-t/\tau)$  where  $\tau \approx 1000$  s. This second time constant  $\tau$  of the system seems to be even longer for lower voltages (for example  $U_{step} = 0.6$  V) since the current does not approach to an asymptotic value even after  $5 \times 10^4$  s. Experiments with  $U_{step} > 0.7$  V lead to a remanent change of the device capacity, hence being disregarded in this work.

With negative values for  $U_{step}$  the shape of the current transients up to  $t = 10$  s is partially similar. The charging domain up to  $t = 10^{-3}$  s as well as the  $\approx t^{-1}$  decay up to 10 s can be seen in the current transient. This decay is also followed by a smooth decrease to the asymptotic value for negative voltages. But, the subsequent increase of the current with large time constants does not appear for voltages  $-0.5 \text{ V} \leq |U_{step}| \leq -0.7$  V. Hence, a second time constant does not exist, when electrons flow from the titanium back electrode to the gold top electrode.

With tantalum devices higher voltages up to 1.4 V in both polarities were possible without changing their dielectric properties.

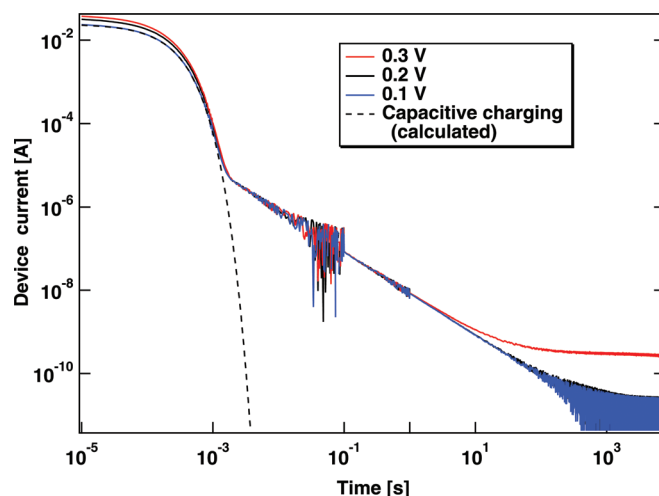


**Figure 10.** (Color online) Transient shape of the device current after voltage steps from 0 V to voltages  $U_{step}$  indicated in the figure. Dotted line: calculated transient shape for  $U_{step} = 0.1$  V according to Eq. 8. Device: Ti/TiO<sub>x</sub> (7.2 nm)/Au.

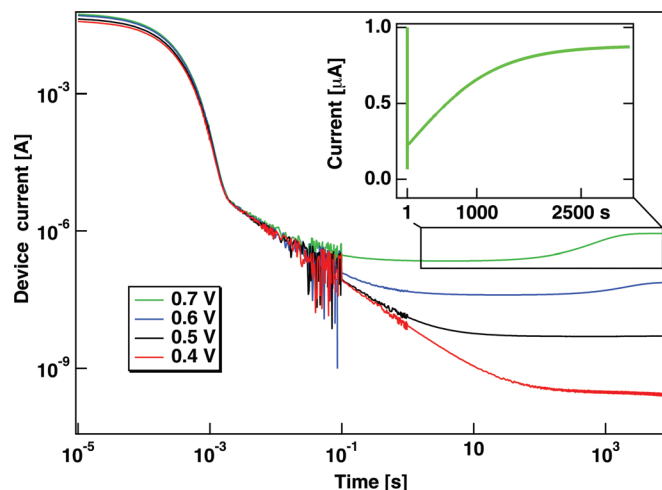


**Figure 11.** (Color online) Transient shape of the device current after voltage steps  $U_{\text{step}} = 0.4\text{--}0.7$  V. Inset: Linear plot of the current transient for  $U_{\text{step}} = 0.7$  V from  $t = 1$  s to  $t = 3000$  s. Device: Ti/TiO<sub>x</sub> (7.2 nm)/Au.

After 10 s the currents remained comparably stable. A second time constant as observed for titanium did not show up. Hence, the current transients are not shown in the present work.

**Steady state currents.**—The steady state currents observed at  $t > 10^4$  s are plotted as a function of the bias voltage in Fig. 12 (open circles for titanium oxide, closed circles for tantalum oxide). The data are compared with elastic tunnel currents calculated for the titanium system for oxide thicknesses of 4.4 and 7.2 nm, as used in the experiment. As barrier parameters we took two value pairs from table 1, i.e.  $E_F(\text{Ti}) - E_{\text{CB}}(\text{TiO}_x) = E_0 = 0.6$  and  $0.9$  eV and  $E_F(\text{Au}) - E_{\text{CB}}(\text{TiO}_x) = E_0 + |\vec{E}_b| \cdot d_{\text{oxide}} = 1.05$  and  $1.27$  eV, as suggested by the optical experiment. A band gap of 3.4 eV as evaluated in Fig. 5 and determined by photoelectron spectroscopy in literature<sup>56,85,86</sup> is assumed for titanium oxide. The tunnel probability through the barrier is evaluated using the WKB approach which is extended for a two-band system<sup>87</sup> in the present work. The current

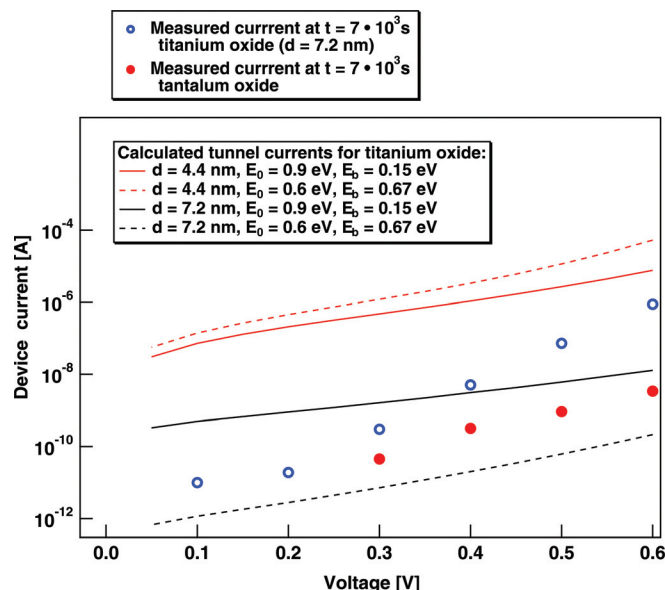


**Figure 12.** (Color online) Steady state device currents as function of bias voltage for titanium (open blue circles) and tantalum oxide (closed red circles). Lines show calculated elastic tunnel currents with two different oxide thicknesses (each with two value pairs for the internal barrier height) for titanium oxide.

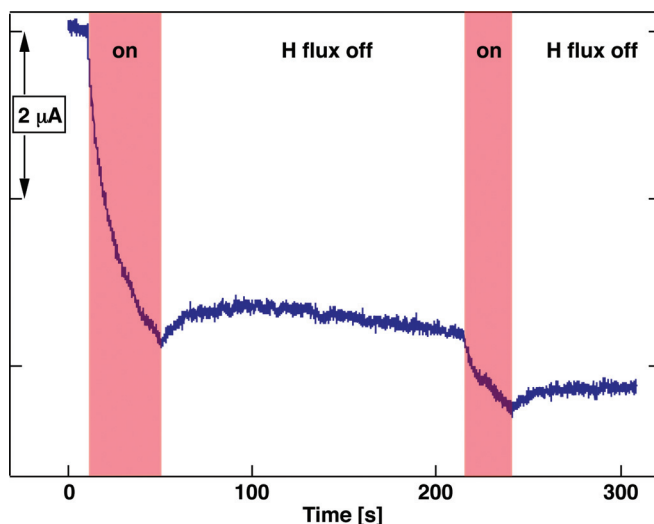


**Figure 13.** (Color online) Transient shape of the induced device current of a Ti/TiO<sub>x</sub> (4.8 nm)/Au (20 nm) device. The atomic hydrogen beam is switched on in the red shaded time intervals. Experiments are accomplished at  $T = 300$  K with an atomic hydrogen flux of  $1 \times 10^{14} \text{ s}^{-1}$ .

density impinging on the barrier is calculated by assuming two half spaces of free Bohr-Sommerfeld electron gases.<sup>6,28,88</sup>

The magnitude of the measured device currents for the 7.2 nm thick titanium oxide samples coincides within 1.5 orders of magnitude with the calculated ones for small bias voltages. However, for  $U_T > 0.3$  V the experimental slope  $\partial \log(I) / \partial U_T$  increases. For  $U_T > 0.5$  V the measured values exceed the range of the calculated values for both barrier types. Hence, it is difficult to explain the experimental results with a constant barrier height. In contrast, a bias-induced additional lowering of the barrier in the course of the experiment must be taken into account for the explanation of the experiments. This bias-induced lowering might be for example driven by a charge exchange of the dipole layers at the two interfaces of the oxide. This process would of course bring a second time constant into the system. The assignment of two processes (fast dielectric charging and slow bias-induced altering of the barrier) is eased when one considers the transient behavior of the device current at higher bias voltages (see Fig. 11).

It should be mentioned that voltage step experiments were also performed with negative values for  $U_{\text{step}}$  (not shown in the previous section). In this case electrons flow from the titanium to the gold top electrode. The lower time constant could be also found. But the current always remained constant after 10 s. A second time constant with values  $\tau > 10$  s did not appear.

The same is valid for tantalum based devices. They only show one time constant in the range of ms in both directions of current flow.

### Chemicurrents

Photoexcitation is one possible way to produce carriers with excess energy in metals. Carriers with excess energy may also be produced in the direct vicinity of a metal surface by the stopping and neutralization of energetic atoms and ions<sup>6,7,89,90</sup> or by nonadiabatic surface chemical reactions.<sup>4,91</sup> We want to use the latter excitation channel to clarify the structure of gold on titanium oxide. One possible interpretation of the resistivity measurements in Sec. II B was a more open and heterogeneous structure of gold on titanium oxide compared to tantalum oxide. In previous experiments the dielectric properties of electronic devices were found to be unchanged under exposure of an atomic hydrogen beam. This was interpreted in terms of a completely covered oxide layer by the top metal gold.<sup>4</sup> The experiments were carried out with an intermitted



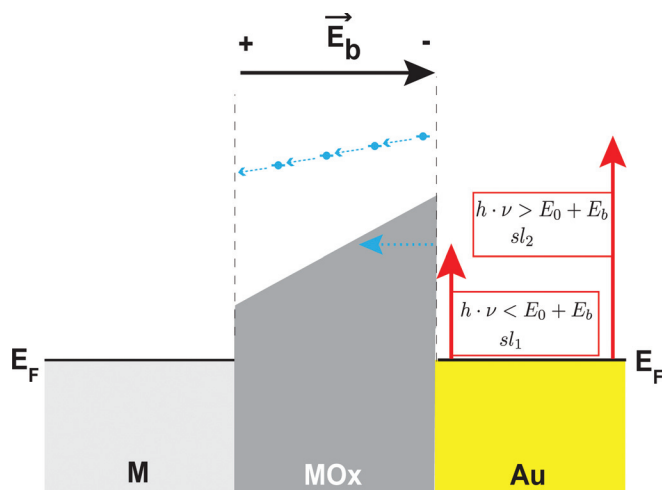


**Figure 14.** (Color online) Model for transport of photoexcited carriers for energies  $h\nu > E_0 + E_b$  and  $h\nu < E_0 + E_b$ .  $sl_1$  and  $sl_2$  denote the slope values from Fig. 5. Transport through the barrier ( $sl_1$ ) can be evaluated by quantum mechanical considerations. Transport through the lower edge of the conduction band ( $sl_2$ ) might be a hindered transport with hopping events (symbolized by dashed arrows between weakly localized states).

atomic hydrogen beam under ultra high vacuum conditions with a tantalum oxide based device. The good repeatability and the unchanged dielectric properties of the device allowed to discuss the current answer of the tantalum oxide based devices as a chemicurrent.<sup>4</sup>

We repeated these chemicurrent experiments with Ti/TiO<sub>x</sub>/Au devices. In Fig. 13 the transient shape of the induced device current can be seen, when the atomic hydrogen beam is switched on at  $t = 10$  s and  $t = 210$  s and switched off at  $t = 50$  s and  $t = 240$  s. The repeated exposure between 210 and 240 s clearly gives different results than the first exposure. Additionally a huge drift of the device current can be observed even when the atomic hydrogen beam is switched off. This behavior is attributed to an hydrogen induced change of the device. Since the gold thickness on tantalum and titanium oxide based devices is the same, we attribute these apparent differences to a leakage of atomic hydrogen through the more open gold layer on the titanium oxide.

The ratio of the induced current of several microampere and the incoming hydrogen atom flux would lead to yields of some 10%. However, a discussion of these device currents in terms of a chemicurrent is not appropriate from our point of view due to the observed device changes.

## Conclusion

It is shown that internal photoemission is a versatile tool for the characterization of internal barriers in heterosystems when a wide range of photon energies is used. The existence of two different slopes ( $sl_1$  and  $sl_2$ , see Fig. 14) in the logarithmic plot of the photoyield versus photon energy enables a clear discrimination between charge transport through a barrier, and above a barrier through the lower edge of a conduction band. The latter process appearing at higher photon energies shows a much weaker dependence on the photon energy than the transport through the barrier, meaning that  $sl_2 < sl_1$  is fulfilled. The value of  $sl_1$  allows the derivation of the barrier parameters by simple quantum mechanical considerations (Eq. 5 and Fig. 6).

A theoretical model for the transport in the lower edge of the conduction band (connected with  $sl_2$ ) cannot be given in the moment. As a transport mechanism we suggest a hindered transport with hopping events between weakly localized states in the smeared out edge of the conduction band.

For titanium oxide samples this hindering can be cancelled out by a small bias voltage ( $< 0.2$  V). This bias leads to a nearly broad band sensitive device meaning that  $sl_2 \approx 0$ .

For tantalum oxide based samples the dependence of the photoyield on the photon energy ( $sl_2$ ) cannot be cancelled out by a bias voltage. This may point to a more stable carrier transport (lower influence by the bias) in the lower edge of the conduction band in tantalum oxide based samples or to a lower density of weakly localized states in the lower edge of the conduction band.

The unusual behavior of the titanium oxide based samples can be found again in the experiments monitoring device currents after the application of voltage steps. The current transients showed complicated structures with two time constants for voltages  $> 0.5$  V. The lower time constant (some milli seconds) is clearly associated with the equilibrium dielectric properties of the device ( $\tau = RC$ ) and is bias-independent, whereas the second time constant (some 10–1000 s) depends on the bias.

To conclude, titanium oxide based devices offer a considerable higher photoyield compared to tantalum oxide based systems. So they seem to be promising candidates for the production of, for example, chemicurrent and photocurrent devices at 0 V bias voltage. However, the complicated bias dependence of the currents driven by internal photo emission or by bias voltages shows the limitations of the field of spectroscopy of internally excited electrons. For this purpose one needs barrier systems which depend in a simple way on the applied bias.<sup>6,7,90</sup>

For titanium oxide samples care has to be taken on changes of the devices during chemicurrent experiments. For reproducible chemicurrent experiments one has to improve the wettability of the oxide for example by a surfactant. With a completely wetted oxide the high sensitivity of titanium oxide based devices will allow the study of chemically induced electronic excitations toward lower energies with metal/insulator/metal devices.

## Acknowledgment

This work is supported by the Deutsche Forschungsgemeinschaft in the frame of the SFB 616 “Energy Dissipation Processes on Surfaces.” K. S. wishes to thank the “Studienstiftung des deutschen Volkes” for support. The authors wish to thank the Institute of Bio- and Nanosystems 2 (Forschungszentrum Jülich) for helping us in the preparation of thin titanium films.

Universität Duisburg-Essen assisted in meeting the publication costs of this article.

## References

1. S. Kamiyama, H. Suzuki, H. Watanabe, A. Sakai, H. Kimura, and J. Mizuki, *J. Electrochem. Soc.*, **141**, 1246 (1994).
2. K.-C. Tsai, W.-F. Wu, C.-G. Chao, and C.-P. Kuan, *J. Electrochem. Soc.*, **153**, G492 (2006).
3. R. Dreiner, *J. Electrochem. Soc.*, **111**, 27 (1964).
4. B. Mildner, E. Hasselbrink, and D. Dising, *Chem. Phys. Lett.*, **432**, 133 (2006).
5. C. L. Platt, B. Dieny, and A. E. Berkowitz, *J. Appl. Phys.*, **81**, 5523 (1997).
6. D. A. Kovacs, J. Winter, S. Meyer, A. Wucher, and D. Dising, *Phys. Rev. B*, **76**, 235408 (2007).
7. D. A. Kovacs, T. Peters, C. Haake, M. Schleberger, A. Wucher, A. Golczewski, F. Aumayr, and D. Dising, *Phys. Rev. B*, **77**, 245432 (2008).
8. D. R. Jennison, P. A. Schultz, and J. P. Sullivan, *Phys. Rev. B*, **69**, 041405 (pages 4) (2004).
9. J. Schäfer, and C. Adkins, *J. Phys.: Condens. Matter*, **3**, 2907 (1991).
10. V. V. Afanas'ev and A. Stesmans, *J. Appl. Phys.*, **102**, 081301 (2007).
11. V. Shvets, V. Aliev, D. Gritsenko, S. Shaimiev, E. Fedosenko, S. Rykhlitski, V. Atuchin, Gritsenko, V. Tapilin, and H. Wong, *J. Non-Cryst. Solids*, **354**, 3025 (2008).
12. K. Kukli, J. Aarik, A. Aidla, O. Kohan, T. Uustare, and V. Sammelselg, *Thin Solid Films*, **260**, 135 (1995).
13. J. Robertson and C. W. Chen, *Appl. Phys. Lett.*, **74**, 1168 (1999).
14. L. Miao, P. Jin, K. Kaneko, A. Terai, N. Nabatova-Gabain, and S. Tanemura, *Appl. Surf. Sci.*, **212–213**, 255 (2003).
15. S. Maeng, L. Axe, T. Tyson, and A. Jiang, *J. Electrochem. Soc.*, **152**, B60 (2005).
16. V. Macagno and J. W. Schultze, *J. Electroanal. Chem.*, **180**, 157 (1984).
17. J. W. Schultze and V. A. Macagno, *Electrochim. Acta*, **31**, 355 (1986).
18. W. Schmickler and J. W. Schultze, in *Modern Aspects of Electrochemistry*, edited by J. O'M. Bockris, B. E. Conway, and R. E. White (Plenum, New York, 1986), No. 17, p. 357.

19. J. W. Schultze and M. M. Lohrengel, *Electrochim. Acta*, **45**, 2499 (2000).
20. K. Stella, D. Bürstel, S. Franzka, O. Posth, and D. Diesing, *J. Phys. D*, **42**, 135417 (2009).
21. K. Stella, D. Bürstel, E. Hasselbrink, and D. Diesing, *Phys. Status Solidi (RRL)*, **5**, 68 (2011).
22. D. Hunkel, M. Marso, R. Butz, R. Arens-Fischer, and H. Lüth, *Mater. Sci. Eng., B*, **69–70**, 100 (2000).
23. Y. Jeliazova, M. Kayser, B. Mildner, A. W. Hassel, and D. Diesing, *Thin Solid Films*, **500**, 330 (2006).
24. A. W. Hassel and M. M. Lohrengel, *Electrochim. Acta*, **42**, 3327 (1997).
25. K. Stella and D. Diesing, *J. Electrochem. Soc.*, **154**, C663 (2007).
26. A. W. Hassel and M. M. Lohrengel, *Electrochim. Acta*, **40**, 433 (1995).
27. J. W. Schultze and A. W. Hassel, in *Encyclopedia of Electrochemistry*, Vol. 4, Section 3.2, pp. 216–270, Wiley-VCH, Weinheim, (2003).
28. D. Diesing, G. Kritzer, M. Stermann, D. Nolting, and A. Otto, *J. Solid State Electrochem.*, **7**, 389 (2003).
29. J. Blakemore, *Solid State Physics*, Cambridge University (1985), p. 152.
30. S. H. Overbury, P. A. Bertrand, and G. A. Somorjai, *Chem. Rev.*, **75**, 547 (1975).
31. C. Bombis, A. Emundts, M. Nowicki, and H. P. Bonzel, *Surf. Sci.*, **511**, 83 (2002).
32. U. Breuer and H. P. Bonzel, *Surf. Sci.*, **273**, 219 (1992).
33. J. C. Heyraud and J. J. Metois, *Acta Metall.*, **28**, 1789 (1980).
34. M. McLean and H. Mykura, *Surf. Sci.*, **5**, 466 (1966).
35. L. Z. Mezey and J. Giber, *Surf. Sci.*, **117**, 220 (1982).
36. E. Bauer, *Zeitschrift für Kristallographie*, **110**, 423 (1958).
37. J. H. van der Merwe and E. Bauer, *Phys. Rev. B*, **39**, 3632 (1989).
38. F. Cosandey and T. E. Madey, *Surf. Rev. Lett.*, **8**, 73 (2001).
39. *CRC Materials Science and Engineering Handbook*, CRC, Boca Raton (2001), p. 253.
40. *CRC Materials Science and Engineering Handbook*, CRC, Boca Raton (2001), p. 254.
41. R. Tadmor, *Langmuir*, **20**, 7659 (2004).
42. I. Olefjord and A. Nylund, *Surf. Interface Anal.*, **21**, 290 (2004).
43. M. Handke, C. Paluszkiwicz, and W. Wyrwa, *Mater. Chem.*, **5**, 199 (1980).
44. A. Grossmann, W. Erley, J. B. Hannon, and H. Ibach, *Phys. Rev. Lett.*, **77**, 127 (1996).
45. A. Grossmann, W. Erley, J. B. Hannon, and H. Ibach, *Phys. Rev. Lett.*, **78**, 3587 (1997).
46. W. Haiss, *Rep. Prog. Phys.*, **64**, 591 (2001).
47. D. Edwards, *Int. J. Heat Mass Transfer*, **25**, 815 (1982).
48. S. Pepper, *J. Opt. Soc. Am.*, **60**, 805 (1970).
49. J. L. Ord and W. P. Wang, *J. Electrochem. Soc.*, **130**, 1809 (1983).
50. J. L. Ord, D. J. D. Smet, and D. J. Beckstead, *J. Electrochem. Soc.*, **136**, 2178 (1989).
51. A. G. Revesz, J. H. Reynolds, and J. F. Allison, *J. Electrochem. Soc.*, **123**, 889 (1976).
52. E. Franke, C. L. Trimble, M. J. DeVries, J. A. Woollam, M. Schubert, and F. Frost, *J. Appl. Phys.*, **88**, 5166 (2000).
53. B. R. Cooper, H. Ehrenreich, and H. R. Philipp, *Phys. Rev.*, **138**, A494 (1965).
54. H. V. Nguyen, I. An, and R. W. Collins, *Phys. Rev. B*, **47**, 3947 (1993).
55. L.-J. Meng, V. Teixeira, H. N. Cui, F. Placido, Z. Xu, and M. P. dos Santos, *Appl. Surf. Sci.*, **252**, 7970 (2006).
56. Y. Wouters, A. Galerie, and J.-P. Petit, *J. Electrochem. Soc.*, **154**, C587 (2007).
57. P. H. P. Koller, H. J. M. Swagten, W. J. M. de Jonge, H. Boeve, and R. Coehoorn, *Appl. Phys. Lett.*, **84**, 4929 (2004).
58. P. H. P. Koller, F. W. M. Vanhelmont, H. Boeve, R. Coehoorn, and W. J. M. de Jonge, *J. Appl. Phys.*, **93**, 8549 (2003).
59. R. Cataliotti, *J. Phys. C*, **7**, 3467 (1974).
60. R. Franchy, *Surf. Sci. Rep.*, **38**, 195 (2000).
61. F. L. Schuermeyer, C. R. Young, and J. M. Blasingame, *J. Appl. Phys.*, **39**, 1791 (1968).
62. F. L. Schuermeyer and J. A. Crawford, *Appl. Phys. Lett.*, **9**, 317 (1966).
63. R. M. Handy, *J. Appl. Phys.*, **37**, 4620 (1966).
64. R. H. Fowler, *Phys. Rev.*, **38**, 45 (1931).
65. V. V. Afanas'ev, M. Houssa, A. Stesmans, and M. M. Heyns, *J. Appl. Phys.*, **91**, 3079 (2002).
66. Z. Rotenberg, Y. Prischepa, and Y. Pleskov, *J. Electroanal. Chem.*, **56**, 345 (1974).
67. Y. V. Pleskov and Z. A. Rotenberg, *J. Electroanal. Chem. Interfacial Electrochem.*, **94**, 1 (1978).
68. Y. V. Gurevich, Y. V. Pleskov, and Z. A. Rotenberg, *Photoelectrochemistry*, Consultants Bureau, Singapore, (1980).
69. Z. A. Rotenberg, N. V. Gromova, and V. E. Kazarinov, *J. Electroanal. Chem. Interfacial Electrochem.*, **204**, 281 (1986).
70. R. H. Fowler and L. Nordheim, *Proc. R. Soc. London*, **119**, 173 (1928).
71. L. Nordheim, *Zeitschrift für Physik*, **46**, 833 (1928).
72. G. Wentzel, *Zeitschrift für Physik A Hadrons and Nuclei*, **38**, 518 (1926).
73. H. A. Kramers, *Zeitschrift für Physik A Hadrons and Nuclei*, **39**, 828 (1926).
74. L. Brillouin, *Compt. Rend.*, **183**, 24 (1926).
75. P. Thissen, B. Schindler, D. Diesing, and E. Hasselbrink, *New J. Phys.*, **12**, 113014 (2010).
76. S. John, C. Soukoulis, M. H. Cohen, and E. N. Economou, *Phys. Rev. Lett.*, **57**, 1777 (1986).
77. F. Urbach, *Phys. Rev.*, **92**, 1324 (1953).
78. J. P. Masse, H. Szymanski, O. Zabeida, A. Amassian, J. E. Klemberg-Sapieha, and L. Martinu, *Thin Solid Films*, **515**, 1674 (2006).
79. K. Stella, D. A. Kovacs, and D. Diesing, *Electrochem. Solid-State Lett.*, **12**, H453 (2009).
80. R. M. Fleming, D. V. Lang, C. D. W. Jones, M. L. Steigerwald, D. W. Murphy, G. B. Alers, Y.-H. Wong, R. B. van Dover, J. R. Kwo, and A. M. Sergent, *J. Appl. Phys.*, **88**, 850 (2000).
81. J. R. Nesbitt and A. F. Hebard, *Phys. Rev. B*, **75**, 195441 (2007).
82. A. K. Jonscher, *J. Phys. D*, **32**, R57 (1999).
83. J. Curie, *Annales de chimie et de physique*, **17**, 385 (1889).
84. E. R. v. Schweidler, *Annalen der Physik*, **329**, 711 (1907).
85. P. M. Kumar, S. Badrinarayanan, and M. Sastry, *Thin Solid Films*, **358**, 122 (2000).
86. J. M. Sanz, L. Soriano, P. Prieto, G. Tyuliev, C. Morant, and E. Elizalde, *Thin Solid Films*, **332**, 209 (1998).
87. K. Gundlach, *J. Appl. Phys.*, **44**, 5005 (1973).
88. C. B. Duke, *Tunneling in Solids*, Academic, New York (1969).
89. D. Kovacs, T. Babkina, T. Gans, U. Czarnetzki, and D. Diesing, *J. Phys. D*, **39**, 5224 (2006).
90. D. Kovacs, A. Golczewski, G. Kowarik, F. Aumayr, and D. Diesing, *Phys. Rev. B*, **81**, 075411 (2010).
91. H. Nienhaus, B. Gergen, H. S. Bergh, A. Majumdar, W. H. Weinberg, and E. W. McFarland, *Phys. Rev. Lett.*, **82**, 446 (1999).